

Low-frequency absorption band in a thin acoustic metamaterial using acoustic black hole termination

Gauthier Bezançon^{a,*}, Maël Lopez^a, Olivier Doutres^a, Raymond Panneton^b, Thomas Dupont^a

^a Department of Mechanical Engineering, École de Technologie Supérieure, Montréal, Québec, H3C 1K3, Canada

^b CRASH-UdeS, Department of Mechanical Engineering, Université de Sherbrooke, 2500 boul. de l'Université, Sherbrooke, Québec, J1K 2R1, Canada

ARTICLE INFO

Keywords:

Sound absorbers
Acoustic metamaterial
Absorption band
Mass-spring representation
Acoustic black hole

ABSTRACT

The proposed metamaterial is a multi-pancake absorber, composed of periodically arranged thin annular cavities, with an alternative main pore profile that combines a constant section and an acoustic black hole termination to achieve an effective absorption band at low frequencies. The constant section at the opening enables low-frequency sound absorption, while the short acoustic black hole termination allows absorption band without a high-frequency shift. An equivalent mass-spring model using a single equivalent stiffness to represent the whole constant main pore section is proposed. This approach simplifies modeling and reduces computation time while capturing the metamaterial's multiple resonances and visualizing mass velocities at resonance frequencies, providing insight into its acoustic behavior. Validation is carried out using thermo-visco-acoustic finite element simulations and impedance tube measurements. First, profiles with an acoustic black hole termination of one to three main pores are studied to gain insight into the formation of combined modes and their impact on absorption. Next, optimizations are performed to achieve broadband absorption, resulting in the two best profiles. The first profile exhibits a 300 Hz absorption band starting at 550 Hz, while the second achieves a broader 500 Hz band at slightly higher frequencies, for a 3-cm thick material.

1. Introduction

Effective noise reduction is a fundamental requirement in today's environment. With increasing urbanization and technological progress, addressing noise pollution has become an essential challenge. Conventional passive acoustic materials, while proficient, often require significant thickness, particularly for low-frequency sound absorption. Additionally, their potential issues related to flammability or concerns about hygiene and health can be constraining in demanding environments. Drawing inspiration from electromagnetic metamaterials [1], acoustic metamaterials offer an effective means to influence wave propagation [2], making them ideal for acoustic absorption. They typically are subwavelength materials, ensuring enhanced absorption at lower frequencies compared to conventional materials of equivalent thickness. Acoustic metamaterial absorbers commonly exhibit a periodic structure composed of diverse elementary resonant cells, including quarter-wavelength structures [3,4], Helmholtz resonators [5–7], membranes [8–11], or more complex elements [12–14].

Expanding on the research conducted by Leclaire et al. [3], Dupont et al. [15] proposed a low-thickness acoustic metamaterial, called

'multi-pancake absorber'. This metamaterial is composed of periodically spaced plates with a constant main perforation, forming very thin annular cavities among themselves. It is demonstrated that at low frequencies, this material exhibits behavior equivalent to a quarter-wave resonator with an increased effective compressibility leading to a reduction in the effective sound speed. Thus, despite its slim thickness (3 cm), this absorber presents a first absorption peak at low frequencies (350 Hz) and multiple absorption peaks at medium frequencies (between 1000 Hz and 2500 Hz). Variations of this geometry have been studied to achieve a lower-frequency first absorption peak while preserving the material's thinness and its multi-absorption peak behavior. This includes using an off-center main pore [16] or replacing the thin cylindrical cavities with annular Helmholtz resonators [17].

Another work [18] investigated the use of acoustic black hole (ABH) profiles within the acoustic metamaterial from reference [15] to achieve broadband absorption. An ABH material corresponds to a structure with a main perforation gradually decreasing from the front to the back of the sample, causing a progressive reduction of the sound celerity and thereby minimizing the reflection of acoustic waves. This type of structure is also referred to as a sonic black hole (SBH) in some studies.

* Corresponding author.

E-mail address: gauthier.bezancon.1@ens.etsmtl.ca (G. Bezançon).

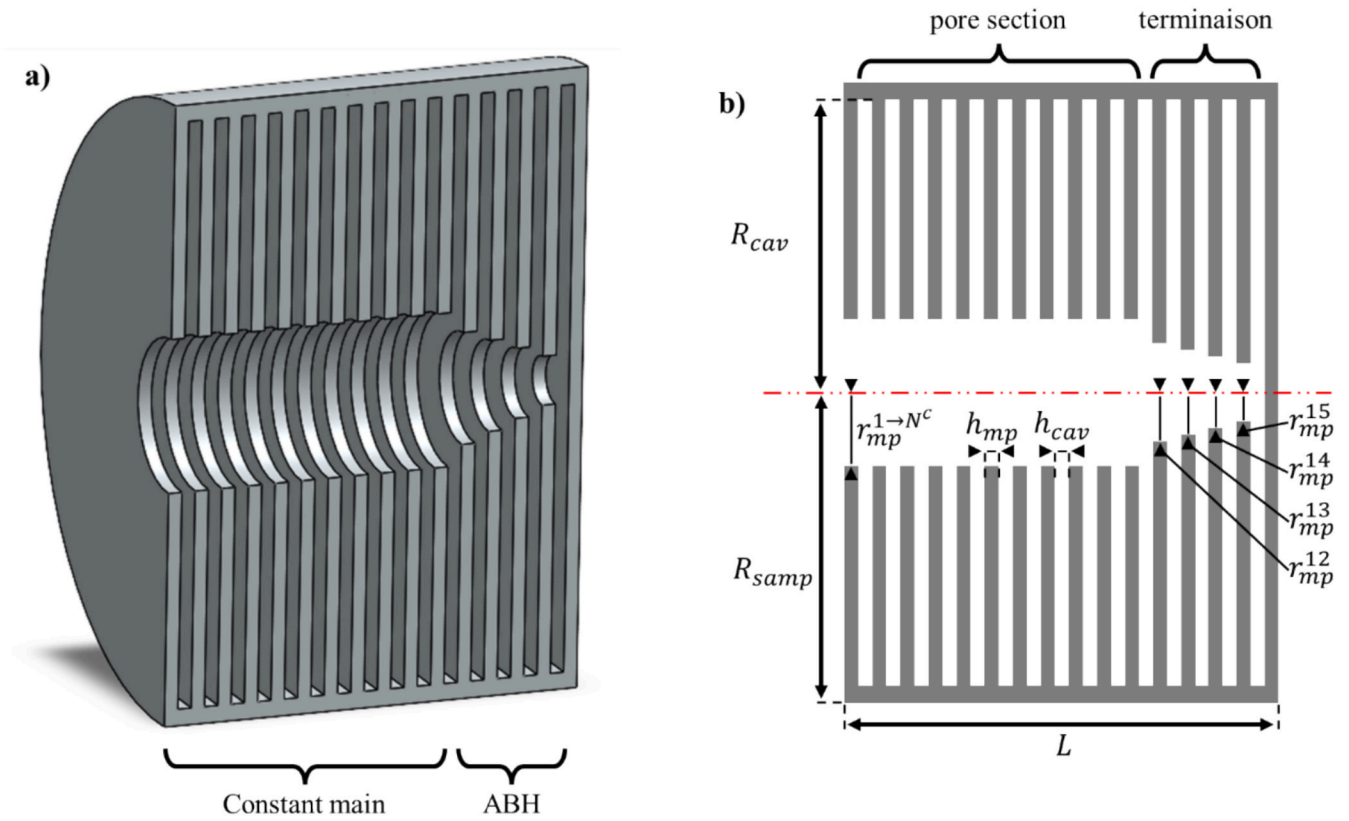


Fig. 1. Visualization of the proposed metamaterial: a) 3D cross-sectional view and b) 2D cross-sectional view.

Initially explored in reference [19], adaptations to various structures have also been proposed [20–24]. Recently, Umnova et al. [25] further examined a lossy ABH structure, highlighting the influence of the local resonances of its inner cavities on the absorption coefficient. This phenomenon has also been investigated through visualizations of sound pressure distributions [26,27]. The advantage of this type of structure lies in its distinct local cavity resonances, which enable the creation of a wide frequency band sound absorption characterized by several closely positioned absorption peaks in frequency. However, these materials are generally bulky, with a significant thickness. Building upon Ref. [25], ABH profiles have been integrated into the thin 'multi-pancake absorber' of 3 cm thickness, and a parametric analysis enhanced the understanding of its acoustic behavior [18]. However, to achieve an efficient broadband absorber with an ABH profile within the acoustic metamaterial from [15], a significative increase in the main pore radius entrance is required, which also shifts the absorption band towards higher frequencies. Therefore, with an ABH profile, a high absorption band is only achieved at relatively high frequencies (above 1 500 – 2 000 Hz) with this thin metamaterial of 3 cm thickness [18].

The objective of this paper is to achieve a lower frequency absorption band compared to that of the ABH profiles, specifically below 1500 Hz, through strategic and slight modifications to the constant profile 'multi-pancake absorber' structure, all while maintaining the material's thickness and size unchanged. For this purpose, combinations of a constant profile with an ABH profile section at the end are investigated. This aims to exploit the low-frequency absorption of the metamaterial with a constant profile [15], while using the combination with the local resonances of the ABH profiles cavities at the end [18] to form a low-frequency absorption band.

Transfer matrix method is widely employed to investigate multi-resonant materials [3,5,6,15,18], enabling straightforward modeling of various geometries. The mass-spring approach can also be used [17,28–30], offering the advantage of easily visualizing resonance mode

deformations, thereby providing a better understanding of the fundamental physical phenomena that govern the acoustic behavior of a material. However, representing a material with numerous resonant cavities results in a high number of degrees of freedom, making the system more complex and time-consuming to solve. This study develops an equivalent mass-spring model, corresponding to a reduced version of the model proposed by Lopez et al [17]. To achieve this, the expressions of equivalent parameters established for the 'multi-pancake absorber' with a constant profile developed in reference [3] and adapted in reference [15], are utilized. These expressions enable the representation of the constant section of the profile with a single equivalent stiffness while modeling its multiple resonances, thereby significantly reducing the system's degrees of freedom. This approach results in a simpler low-frequency model while still allowing for the visualization of mass velocities at resonance frequencies.

The paper is organized as follows. In **section 2**, the metamaterial structure is described, and the equivalent mass-spring model is detailed. Next, in **section 3.1**, the proposed analytical model is verified on the constant-profile metamaterial with finite element model (FEM) simulations and measurements. Then, in **section 3.2**, the formation of combined modes in low-frequency is analyzed thanks to the visualization of mass velocities, using profiles that combine a constant section with an ABH termination of one to three main pores. Finally, in **section 3.3**, the studied profiles are optimized to achieve a material with a low-frequency absorption band, and the two best profiles are described.

2. Material and methods

2.1. Material

The metamaterial under investigation is the 'multi-pancake absorber' with an alternative profile (see Fig. 1), consisting of a constant main pore section in the major part of the profile combined with an ABH

Table 1
Dimensions of the constant geometric parameters of the material.

Parameters	h_{mp}	h_{cav}	L	R_{cav}	R_{samp}	N
Value	1 mm	1 mm	31 mm	21 mm	22.22 mm	15

termination, i.e., with a few modified main pores at the end.

The structure is composed of $N+1$ periodically spaced plates, each with a main perforation, called here ‘‘main pore’’ and denoted ‘‘mp’’, except for the last plate, which has no perforation and serves as a rigid termination. These plates form N thin cylindrical cavities between them. The thickness of each main pore is h_{mp} and that of each cavity is h_{cav} . Thus, the total thickness of the material is $L = (N+1)h_{mp} + Nh_{cav} = (h_{mp} + h_{cav})N + h_{mp}$. The overall geometry is a circular cylinder with a radius R_{samp} , and all the cavities have a radius R_{cav} . All values of these geometric parameters are summarized in Table 1 and remain constant throughout this study. They have been chosen to be consistent with the geometry previously investigated in earlier studies (see Sample B in reference [15] and materials in reference [18]).

The variable parameters in this work are limited to those that define the main pore profile. The profile under investigation consists first of a constant section composed of N^c main pores with an $r_{mp}^{1 \rightarrow N^c}$ radius. Then, the final section of the profile, the ABH termination, is composed of a few modified main pores, where the radius of the i^{th} main pore is denoted as r_{mp}^i , with i ranging from $N^c + 1$ to N . For instance, the profile of the metamaterial shown in Fig. 1, is defined by $r_{mp}^{1 \rightarrow N^c}$ with $N^c = 11$, and r_{mp}^{12} , r_{mp}^{13} , r_{mp}^{14} and r_{mp}^{15} for the ABH termination. As mentioned previously, this profile aims to take advantage of the local resonances in these cavities, while avoiding the shift towards high frequencies observed in a complete ABH profile due to all modified main pores [18].

2.2. Equivalent mass-spring model

Based on the reference [17], an equivalent mass-spring model is proposed to model the acoustic behaviour of the metamaterial with the studied profile. The term ‘‘equivalent’’ refers to the fact that the section with a constant profile is modeled with a single mass, which represents the first main pore, and a single stiffness, which represents the rest of the constant profile material thanks to a low-frequency approximation of its compressibility. This reduces the analytical complexity of the problem, reduces resolution time, and represents the behavior of this multi-resonant metamaterial in a simpler and more understandable manner while modeling all its multiple resonances. Conversely, the ABH termination at the end of the profile is conventionally modeled, with each modified main pore described as a mass and each cavity between them described as a spring. Fig. 2 presents an example of a material constituted of a profile composed of a constant section of 11 main pores followed by an ABH termination composed by 4 modified main pores, as the material shown in Fig. 1. This material is only modeled by a 5 mass-

spring system. In general, the proposed metamaterial with a profile composed of a constant section of N^c main pores and $N^k = N - N^c$ modified main pores, is modeled by a $N^k + 1$ mass-spring system.

Note that simulations using a ‘‘15 mass-spring system’’ model were conducted on the various materials of this study (not shown for conciseness) and, while nearly identical below 2000 Hz, corresponding to our frequency range of interest, they align more closely with the FEM results above this frequency.

2.2.1. Masses description for the main pores

In a mass-spring analogy, the masses describe the inertia of a part of the studied system. The first mass, denoted as M_1 , is associated to the first main pore at the front of the material and it is expressed as follows

$$M_1 = \rho_{mp}^1 A_{mp}^1 h_{mp}^1 \quad (1)$$

where ρ_{mp}^1 is the effective main pore density, $A_{mp}^1 = \pi r_{mp}^1{}^2$ the main pore cross-section area and h_{mp}^1 the equivalent main pore thickness. The effective density ρ_{mp}^1 is given by the Johnson-Champoux-Allard (JCA) model, detailed in [31], which allows for the consideration of thermal and viscous losses at the pore walls. Main pores are identified to circular cross-section pores and the corresponding parameters are detailed in Table 2. End correction is used to account for radiation effect in front side of the first main pore $h_{mp}^1 = \delta_1^1 + h_{mp}$, where δ_1^1 is Karal end corrections [32]. The subsequent masses, denoted as M_k with k ranging from 2 to $N^k + 1$, are associated with the few modified main pores at the end of the profile. Thus, the k^{th} mass is associated with the i^{th} main pore, with $i = N^c - 1 + k$. These masses are expressed as follows

$$M_k = \rho_{mp}^i A_{mp}^i h_{mp}^i \quad (2)$$

where ρ_{mp}^i is the effective main pore density, $A_{mp}^i = \pi r_{mp}^i{}^2$ the main pore cross-section area and $h_{mp,i}^i$ the equivalent main pore thickness. The effective density ρ_{mp}^i is given by the JCA model [31] to consider thermal and viscous losses (see parameters in Table 2). End corrections are also

Table 2

Johnson-Champoux-Allard (JCA) parameters [31], with η the dynamic viscosity of air.

JCA parameters	Porosity Φ	Tortuosity α_∞	Viscous length Λ (m)	Thermal length Λ' (m)	Static air flow resistivity σ (Pa·s/m ²)
Main pore (circular pore)	1	1	r_{mp}^i	r_{mp}^i	$8\eta/r_{mp}^i{}^2\Phi$
Annular cavity (slit)	1	1	h_{cav}	h_{cav}	$12\eta/h_{cav}{}^2\Phi$

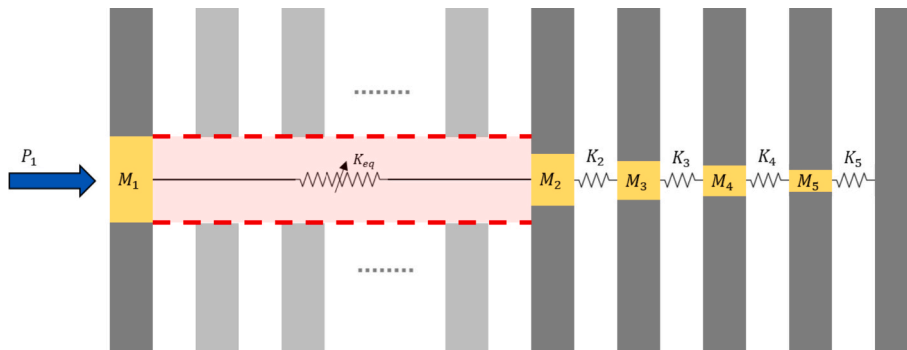


Fig. 2. Representation of the equivalent mass-spring model for the proposed material.

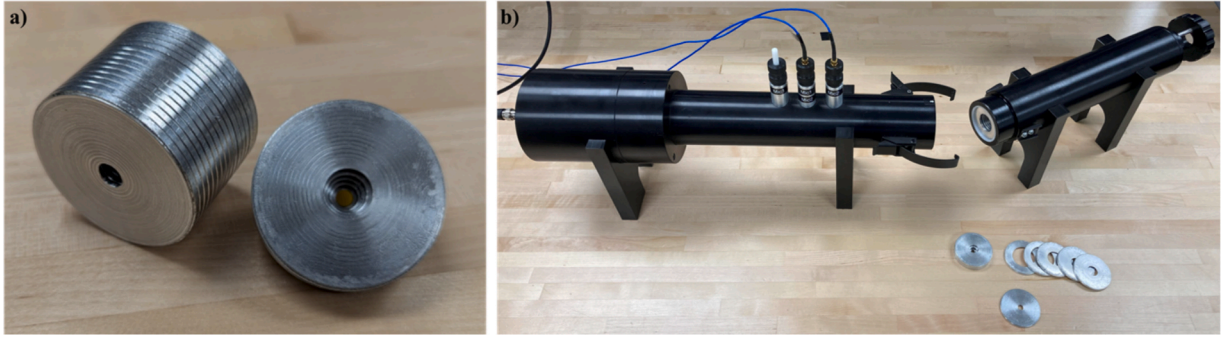


Fig. 3. Photographs of a) a complete sample composed of 15 assembled elements (left) and an ABH termination consisting of 5 elements (right); and b) the impedance tube used for measurements, shown open with a sample inside.

used to account for radiation effect on cavities on both sides of each main pore $h_{mp}^i = \delta_1^i + h_{mp} + \delta_2^i$, where δ_1^i and δ_2^i are Karal end corrections [32]. End corrections are limited here by half of the thin cavities thickness $\delta_{max} = h_{cav}/2$, except for $\delta_1^{N^c+1}$ which is not limited and corresponds to the end correction from the second mass to the equivalent pore.

2.2.2. Equivalent stiffness description for the constant section

In this mass-spring model, the constant main pore section of the profile is described by the mass M_1 , representing the first main pore, and a single equivalent stiffness K_{eq} , representing the remaining constant main pore section (i.e. N^c cavities and $N^c - 1$ main pores), defined by

$$K_{eq} = j\omega A_{mp}^1 Z_{cst} \quad (3)$$

where Z_{cst} is the acoustic impedance matrix relating the acoustic pressure and the acoustic velocity at the entry (1) and exit (2) of the constant main pore section: $\begin{bmatrix} P_1 \\ P_2 \end{bmatrix} = Z_{cst} \begin{bmatrix} V_1 \\ V_2 \end{bmatrix}$. It can be determined using the transfer matrix T_{cst} , as demonstrated in Appendix A, and its expression is given by

$$Z_{cst} = \begin{bmatrix} -jZ_{eq} \cot(k_{eq}L_{cst}) & jZ_{eq} / \sin(k_{eq}L_{cst}) \\ -jZ_{eq} / \sin(k_{eq}L_{cst}) & jZ_{eq} \cot(k_{eq}L_{cst}) \end{bmatrix} \quad (4)$$

where Z_{eq} is the equivalent characteristic impedance, k_{eq} the equivalent wavenumber and $L_{cst} = N^c(h_{cav} + h_{mp}) - h_{mp}$ the thickness of the whole constant section without the first main pore (already taken into account in M_1). The equivalent characteristic impedance is given by $Z_{eq} = \sqrt{\frac{\rho_{mp}}{C_{eq}}}$ and the equivalent wavenumber is given by $k_{eq} = \omega \sqrt{\rho_{mp} C_{eq}}$, where $\rho_{mp} = \rho_{mp}^1$ is the effective density of the main pore given by the JCA model [31] (see parameters in Table 2) and where C_{eq} is the equivalent compressibility of the constant main pore section. Building upon the work of Leclair et al. [3], Dupont et al. [15] provided an expression for the equivalent compressibility (C_{eq}) of a 'multi-pancake absorber' with a constant profile. The expression is notably obtained under the assumption of low frequencies, $\text{Re}(k_{mp}(h_{cav} + h_{mp})) \ll 1$, and the condition that the cavities are much thinner (h_{cav}) compared to their depth (R_{cav}). This expression can be rewritten as

$$C_{eq} = C_{mp} + \frac{1}{j\omega(h_{cav} + h_{mp})} \frac{A_{cav}}{A_{mp}} \frac{1}{Z_{S,cav}} \quad (5)$$

where C_{mp} is the effective compressibility of the main pore given by the JCA model [31] (see parameters in Table 2), A_{cav} and A_{mp} the cross-section area of the cavity and the main pore. $Z_{S,cav}$ is the surface impedance of a thin annular cavity, and its expression is given from [34]

$$Z_{S,cav} = jZ_{cav} \frac{H_0^{(1)}(k_{cav}r_{mp}) - H_0^{(2)}(k_{cav}r_{mp}) H_1^{(1)}(k_{cav}R_{cav})/H_1^{(2)}(k_{cav}R_{cav})}{H_1^{(1)}(k_{cav}r_{mp}) - H_1^{(2)}(k_{cav}r_{mp}) H_1^{(1)}(k_{cav}R_{cav})/H_1^{(2)}(k_{cav}R_{cav})} \quad (6)$$

where $H_a^{(b)}$ is the Hankel function of ath order and bth kind, Z_{cav} is the equivalent characteristic impedance of the annular cavity and k_{cav} its equivalent wavenumber. Z_{cav} and k_{cav} are given by the JCA model [31] to take into account viscous and thermal losses. The thin annular cavities are identified to slits and the corresponding parameters are detailed in Table 2.

2.2.3. Stiffness description for the thin cavities

In the ABH termination, the thin cylindrical cavities positioned after the few modified main pores are also described by springs. First, each of these cavities is represented by two cylindrical junction pores and a thin annular cavity, as done in reference [18]. The two junction pores are of thickness $h_{cav}/2$ and extend from the preceding and following main pores. Positioned between them, the annular cavity is defined with outer radius R_{cav} and inner radius r_{in}^i , obtained through an arithmetic mean $r_{in}^i = (r_{mp}^i + r_{mp}^{i+1})/2$ to most accurately represent the resonant volume. It is described by a lump element, using the expression of the surface impedance $Z_{S,cav}^i$ from reference [34], which corresponds to Eq. (4), replacing r_{mp} by r_{in}^i . Assuming continuity of pressure at the interface between the junction pores and the annular cavity, the surface impedance of the whole cylindrical cavity is given by

$$Z_{S,junction+cav}^i = \frac{A_{in}^i}{\frac{j k_0 V_j}{Z_0} + \frac{A_{cav}^i}{Z_{S,cav}^i}} \quad (7)$$

where Z_0 and k_0 are the characteristic impedance and the wavenumber of the air, $V_j = \pi r_{in}^i{}^2 h_{cav}$ the volume of the inner junction cylinder, $A_{in}^i = \pi r_{in}^i{}^2$ its cross-section and $A_{cav}^i = 2\pi r_{in}^i h_{cav}$ the contact area between the inner junction cylinder and the annular cavity. Then, the k^{th} spring associated with the i^{th} whole cylindrical cavity, with $i = N^c - 1 + k$ (with $k \geq 2$), is defined by

$$K_k = j\omega A_{mp}^i Z_{S,junction+cav}^i \quad (8)$$

Note that $Z_{S,junction+cav}^i$ is also used in the following analysis to determine the resonant frequency of the i^{th} cavity (denoted f_{res}^i). It corresponds to the frequency where the imaginary part of $Z_{S,junction+cav}^i$ equal to zero [18].

2.2.4. Acoustic indicators

With all the defined elements to complete the global mass matrix \mathbf{M} and the global stiffness matrix \mathbf{K} , the acoustic behavior of the proposed metamaterial can be characterized by the matrix equation of size $N^k + 1$

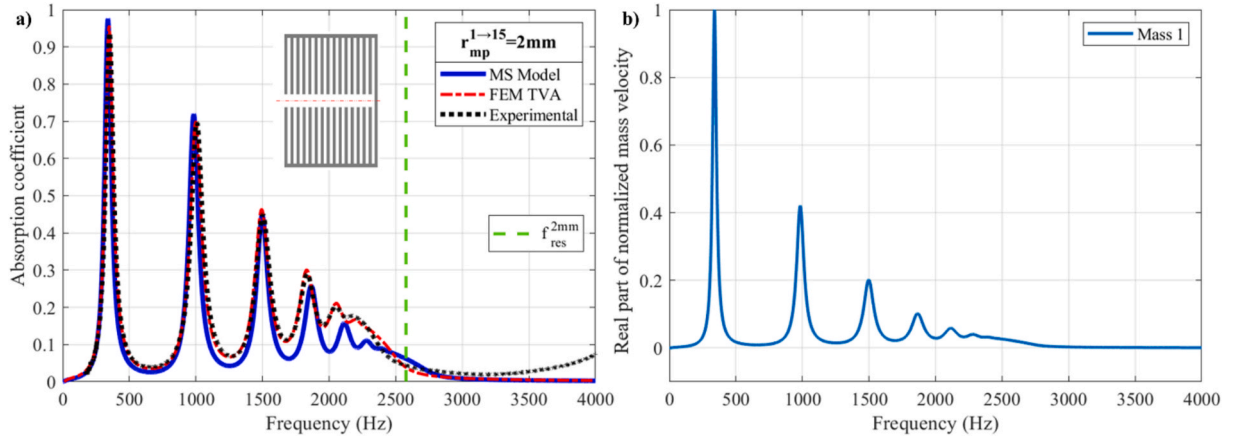


Fig. 4. a) Comparison of the absorption coefficient for a metamaterial with constant profile with $r_{mp}^{1-15} = 2$ mm according to the equivalent mass-spring model, the FEM and experimental results; b) Velocity of mass 1 against frequency from the equivalent mass-spring model.

These elements are designed to minimize air leakage through contact areas. The precision machining provides flatter and smoother surfaces compared to 3D printing, which is crucial for accurately reproducing designed geometries such as cylindrical main pores and annular cavity walls, where losses are concentrated. The smallest achievable main pore

radius using this manufacturing method is 0.4 mm. Experimental measurements are conducted in an impedance tube with a radius $R_{samp} = 22.22$ mm, as shown in Fig. 3 b). The two-microphone method is also used to calculate the normal incidence sound absorption coefficient [35]. The sound absorption measurements use white noise with a global

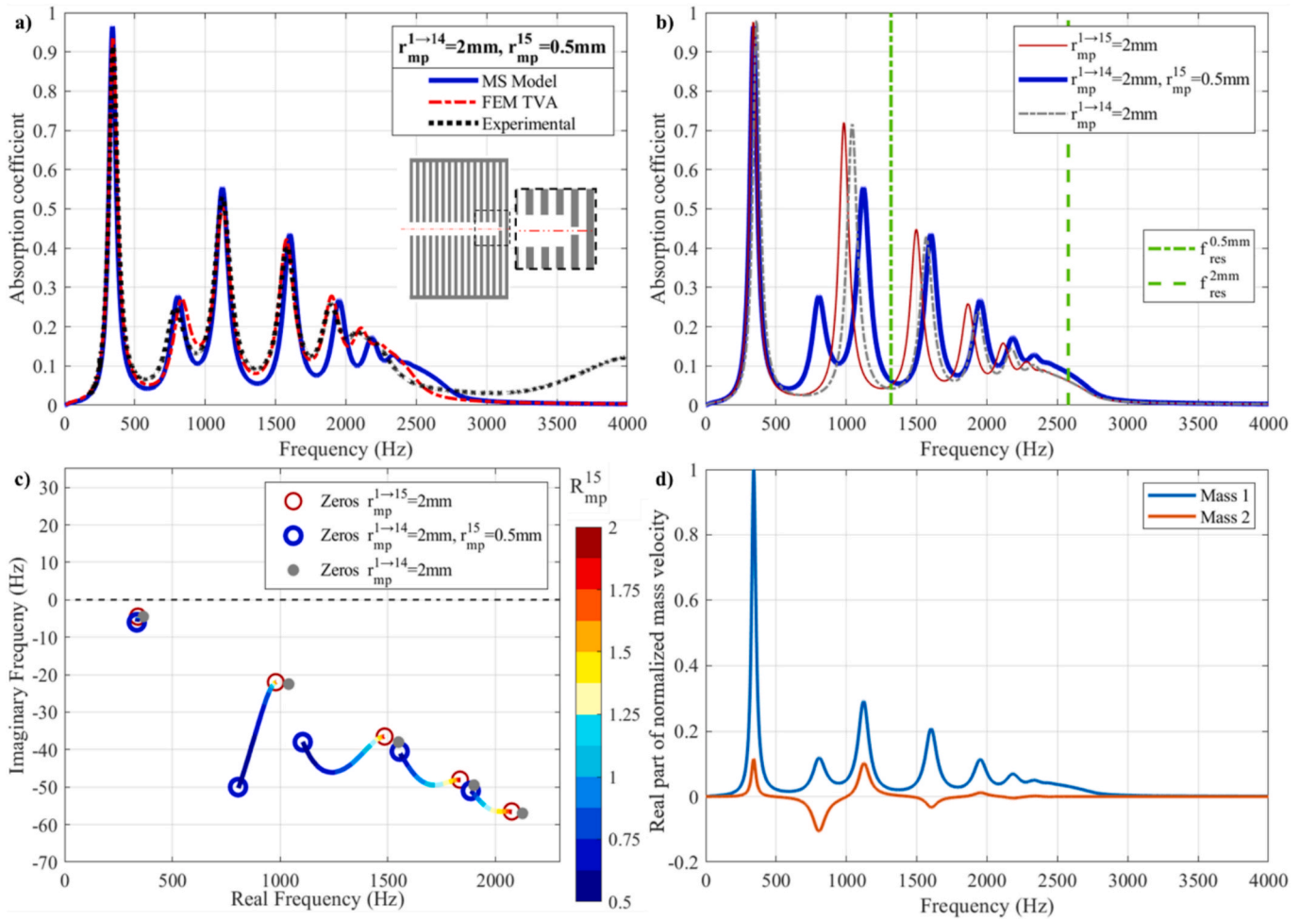


Fig. 5. a) Comparison of the absorption coefficient for the studied metamaterial, with $r_{mp}^{1-14} = 2$ mm and $r_{mp}^{15} = 0.5$ mm, according to the equivalent mass-spring model, the FEM and experimental results; b) Comparison of the absorption coefficient for the studied metamaterial with constant profile metamaterials $r_{mp}^{1-15} = 2$ mm and $r_{mp}^{1-14} = 2$ mm; c) Evolutions of the first five zeros when r_{mp}^{15} varies from 2 to 0.5 mm with $r_{mp}^{1-14} = 2$ mm in the complex frequency plane representation; d) mass velocities of the studied metamaterial against frequencies.

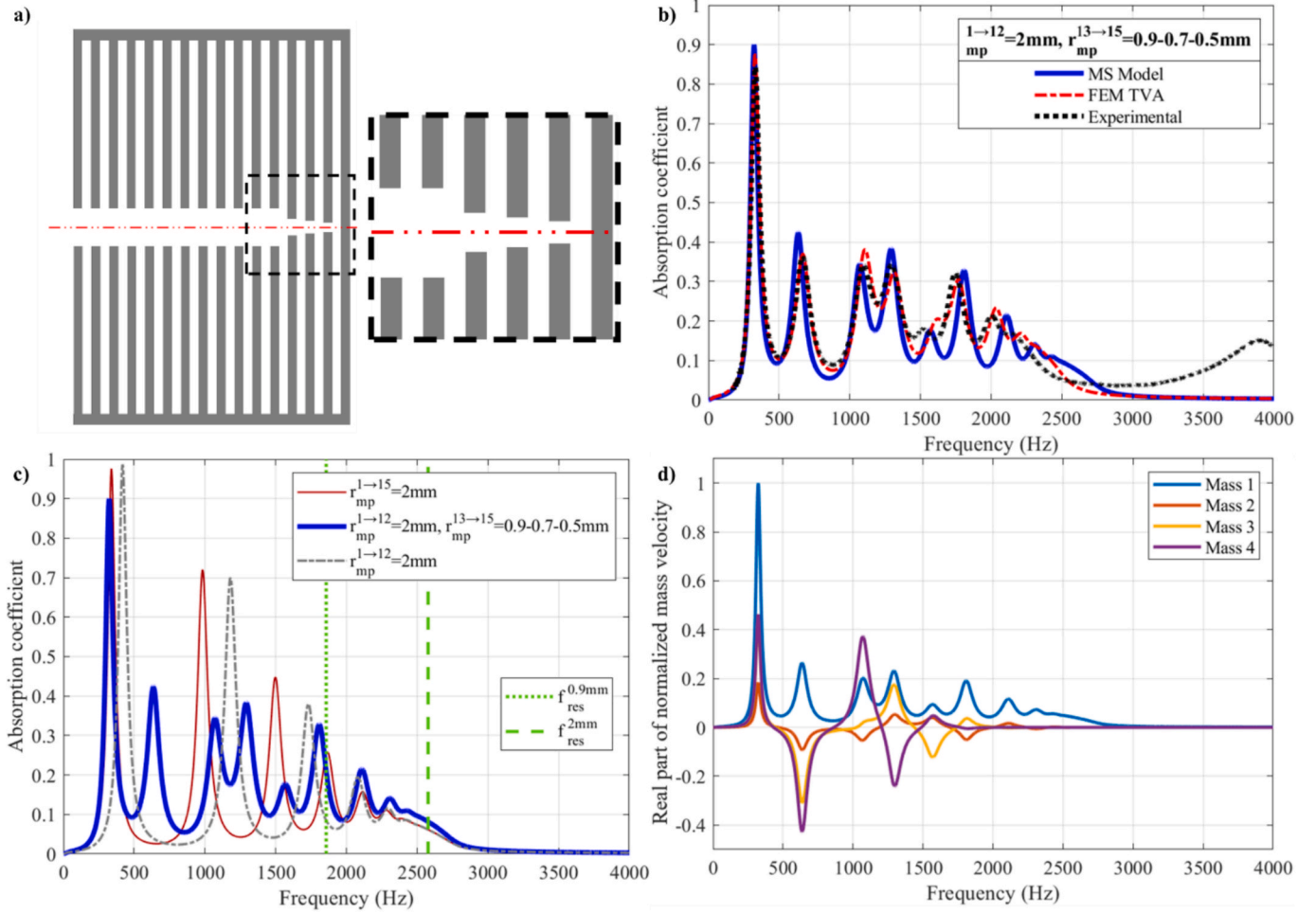


Fig. 6. a) Visualization of the proposed metamaterial over a 300-Hz frequency band with $r_{mp}^{1-12} = 2\text{ mm}$, $r_{mp}^{13} = 0.9\text{ mm}$, $r_{mp}^{14} = 0.7\text{ mm}$ and $r_{mp}^{15} = 0.5\text{ mm}$; b) Comparison of its absorption coefficient according to the equivalent mass-spring model, the FEM and experimental results; c) Comparison of its absorption coefficient with constant profile metamaterials $r_{mp}^{1-15} = 2\text{ mm}$ and $r_{mp}^{1-12} = 2\text{ mm}$; d) Its mass velocities against frequencies.

sound pressure level of 90 dB. Each sample is randomly reconstructed and repositioned for at least five tests to ensure repeatability, and the presented curves, referenced as ‘Experimental’, correspond to their average.

3. Results

3.1. Validation of the equivalent mass-spring model for a constant profile metamaterial

In this section, the proposed equivalent mass-spring model is applied to a constant main pore metamaterial, which serves as a reference for the subsequent profiles under investigation. This whole metamaterial is only modeled by a single mass M_1 , which represents the first main pore, and a single stiffness K_{eq} , which represents the rest of this constant profile metamaterial.

The absorption coefficient of the metamaterial with a constant profile $r_{mp}^{1-15} = 2\text{ mm}$, is depicted in Fig. 4 a), according to the equivalent mass-spring model, the FEM TVA, and the experimental measurements. This profile has been presented in reference [15] and further examined in reference [18]. The equivalent mass-spring model yields results closely aligned with both the FEM TVA and experimental measurements up to 1500 Hz. However, beyond the fourth peak, a gradual shift toward higher frequencies is observed, along with a decrease in the absorption coefficient. This small discrepancy can be attributed to the low-frequency assumption inherent in the equivalent mass-spring model,

leading to a less precise representation of the constant section of the main pore profile at higher frequencies. Nevertheless, even beyond 1500 Hz, the absorption curve remains coherent, maintaining a consistent number, frequency position and amplitude of absorption peaks. It is worth noting that this study focuses on investigating main pore profiles to achieve a lower frequency absorption band compared to that of the ABH profiles, i.e. below 1500 Hz here for a sample thickness of 31 mm and a sample outer radius of 22.22 mm. In this context, the developed model proves well-suited and coherent. Additionally, the resonance frequency of the first cavity, denoted $f_{res}^{2\text{mm}}$, is indicated by a vertical dashed green line. This frequency is calculated using Eq. (7) and corresponds to the start of the band gap. It has been demonstrated that beyond its resonance frequency, a thin cavity behaves as a rigid termination, making the section further back in the material ineffective [18]. In the following, this is used to better understand the acoustic behavior of various profiles metamaterial.

Fig. 4 b) depicts the acoustic velocity of the (sole) mass of the system as a function of frequency. It corresponds to the real part of the derivative of the acoustic displacement of the mass, normalized by the maximum value of velocity: $v_k = Re(j\omega x_k) / |v_{max}|$. The acoustic displacement is directly calculated by solving Eq. (9). Visualizing the acoustic velocity of a mass aids in understanding and identifying resonance modes, as it directly corresponds to the acoustic velocity at the corresponding main pore. Firstly, it can be observed that although the system consists of a single mass and a single equivalent stiffness, it exhibits multiple resonances as expected due to the definition of K_{eq} .

Furthermore, the mass logically reaches maximum velocity at each absorption peak frequency, consistent with the behavior of the mass in a quarter-wave system (see Fig. 10 a-d) in Appendix B and Fig. 6 in reference [17]). Also, it can be noted that the velocity of the mass is positive, indicating that it is in phase with the excitation. Indeed, it has been verified that the imaginary part of the velocity is zero for each maximum velocity, and thus at each resonance, and this is the case for all masses in all profiles of this study. In the subsequent part of the study, this visualization will facilitate the characterization of modes and the assessment of specific mass effects in comparison to other masses, especially in systems with multiple masses.

This section has validated the modeling of a 'multi-pancake absorber' with a constant main pore profile with a reduced system consisting of a single mass and a single equivalent stiffness frequency dependent. Additionally, it introduced the mass velocity visualization. The influence of modifying main pores at the end of the profile on the acoustic behavior of the metamaterial will now be investigated, aiming to improve low-frequency absorption.

3.2. Combined modes analysis

In this section, the investigation focuses on the formation of combined modes and their impact on absorption. In this study, 'combined modes' denotes the modes affected by the combination of both the constant section and the ABH termination. To better understand their behavior, profiles with a few modified main pores at the end of a constant section are analyzed using mass velocity visualization. First, a profile with a single main pore termination is studied. Then, constant profiles with an ABH termination composed of three main pores are analyzed to understand the formation of multiple combined modes and their positive impact on low-frequency sound absorption.

3.2.1. Single main pore termination

The previously examined constant profile is slightly modified by reducing the radius of the last main pore. The profile parameters are defined as $r_{mp}^{1-14} = 2$ mm and $r_{mp}^{15} = 0.5$ mm, and thus the material is represented by two masses, M_1 and M_2 , and two stiffnesses, K_{eq} and K_2 . The absorption coefficient of this profile is shown in Fig. 5 a), according to the equivalent mass-spring model, the FEM TVA, and the experimental measurements. Similar to the constant profile metamaterial (see previous section), the equivalent mass-spring model closely aligns with both FEM TVA and experimental results up to 1800 Hz. The frequency positions of the fourth first peaks are nearly identical across models, with slight differences observed only in their amplitudes. For the subsequent peaks, the equivalent mass-spring model still exhibits a slight shift towards higher frequencies. Nevertheless, the results are very satisfactory, confirming the validity of the observations and conclusions of this section.

Then, in Fig. 5 b), the absorption coefficient of the studied profile (shown in blue) is compared with that of the constant profile from the previous section with 15 main pores (denoted as $r_{mp}^{1-15} = 2$ mm, shown in red), and the same constant profile but composed of only 14 main pores (denoted as $r_{mp}^{1-14} = 2$ mm, shown in dashed gray). In this figure, and in the following one, all curves are computed using the equivalent mass-spring model. It can be observed that reducing the size of the last main pore shifts the absorption peaks towards lower frequencies, changing from two absorption peaks below 1300 Hz (346 Hz and 984 Hz in red) to three peaks (344 Hz, 806 Hz, and 1121 Hz in blue). Additionally, the amplitude of the second absorption peak is significantly reduced (from 0.72 at 984 Hz in red to 0.28 at 806 Hz in blue), while the amplitudes of the subsequent peaks are slightly improved. Additionally, all three profiles exhibit a band gap starting at the same frequency, initiated at the resonance frequency of their identical first cavity [18], denoted as f_{res}^{2mm} (vertical dashed green line), as this cavity is surrounded by 2 mm-radius main pores. Furthermore, the resonance frequency of

the last cavity of the studied profile is denoted as $f_{res}^{0.5mm}$ (vertical dash-dot green line) as it is preceded by a 0.5 mm-radius main pore. Notably, beyond this frequency, the absorption coefficient of the studied "non-constant profile" (depicted in blue) closely resembles that of the constant profile with 14 main pores (in dashed gray). This similarity can be attributed to the behavior of a cavity acting as a rigid termination beyond its resonance frequency ([18;25]). Hence, for frequencies beyond the resonance frequency of its last cavity, the metamaterial under study behaves as if it were solely composed of its first 14 cavities.

The complex frequency plane representation in Fig. 5 c) provides additional insights into the evolution of the acoustic behavior of the metamaterial as it transitions from the reference profile to the profile studied in this section by modifying last main pore radius r_{mp}^{15} from 2 mm to 0.5 mm. The first zero is minimally affected as the first peak of the three profiles is almost identical. All the following zeros shift progressively towards lower frequencies, aligning with the observations in Fig. 5 b). The second zero moves away from the real frequency axis, aligning with the reduced absorption amplitude, due to having excessive loss initially (the zero is below the real frequency axis). Reducing the last main pore increases these losses, shifting the zero downward. Additionally, this zero moves minimally when r_{mp}^{15} changes from 2 to 1 mm but shift significantly when r_{mp}^{15} changes from 1 to 0.5 mm, due to the non-linear increase in losses as the radius decreases. The subsequent three zeros initially move away from the real frequency axis or remain at a consistent distance due to increased losses. They then gradually ascend towards the zeros of the constant profile with 14 main pores (marked in grey) as the 15th main pore decreases. The third zero moves less than the fourth and fifth because it is at a lower frequency, still influenced by the last cavity.

The velocities of the two masses of the studied profile are plotted as a function of frequency in Fig. 5 d). These correspond to the real part of the velocities, normalized by the maximum value of the two. As seen in section 2.2, the first mass corresponds to the first main pore, and the second mass corresponds to the modified main pore, here to the fifteenth main pore. It can be observed that, for the first, third, and fifth resonances, the two masses are in phase with the excitation (both positive), and thus in phase with each other. Conversely, for the second, fourth, and sixth resonances, the first mass is in phase with the excitation (positive) while the second mass is out of phase (negative), making them out of phase with each other. This aligns with the observations in Fig. 6 of reference [17], incorporating a node at each resonance, causing the last mass (in orange) to alternate between being in phase and out of phase with the first mass (in blue). The velocity of the first mass is altered compared to Fig. 4 b), with its amplitude for the second resonance significantly reduced. Furthermore, the second mass exhibits notable velocity for the first three resonances but is significantly reduced at higher frequencies. This aligns with the observations in Fig. 5 b) where the influence of the last main pore only happens before the resonance frequency of the subsequent cavity, corresponding to the first three absorption peaks. Thus, these first three resonances are combined modes, resulting from the interaction between the constant section and the ABH termination (here composed of a single main pore), whereas the subsequent resonances depend almost exclusively on the constant section. It can be noted that among the three combined resonances of this metamaterial, the second resonance depends more on the last main pore than the first and third resonances, as the second mass has an amplitude more similar to the first.

An additional interpretation of the acoustic behavior of this metamaterial with a single main pore termination can be made by visualizing the pressure fields at the resonances, as presented in Fig. 10 e-h) in Appendix B.

Therefore, reducing the last main pore at the end of a constant section shifts the absorption peaks towards lower frequencies without changing the material's thickness and external radius. The last main pore influences only the low-frequency peaks, corresponding to

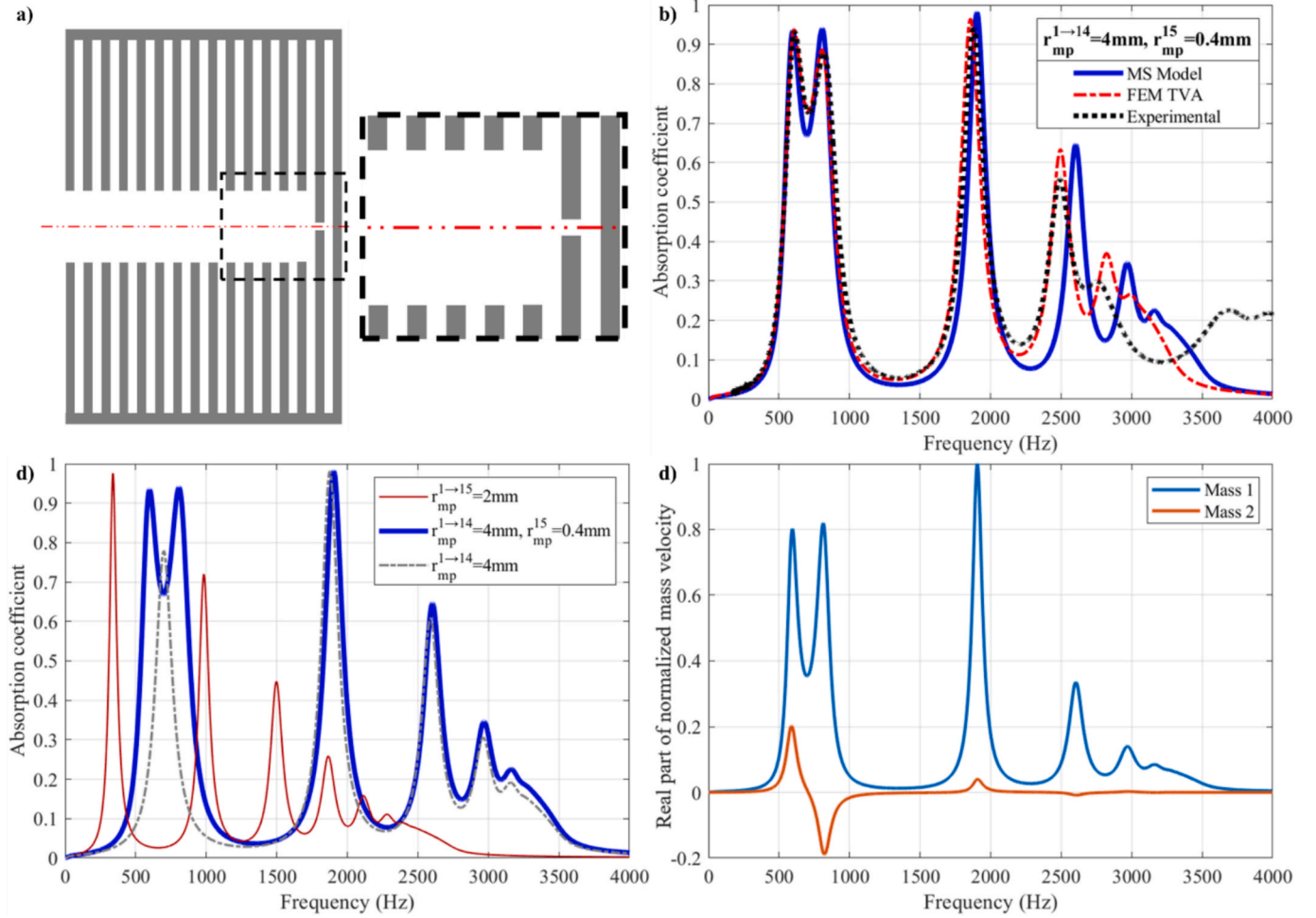


Fig. 7. a) Visualization of the first optimized metamaterial over a 500-Hz frequency band with $r_{mp}^{1-14} = 4$ mm and $r_{mp}^{15} = 0.4$ mm; b) Comparison of its absorption coefficient according to the equivalent mass-spring model, the FEM TVA and experimental results; c) Comparison of its absorption coefficient with constant profile metamaterials $r_{mp}^{1-15} = 2$ mm and $r_{mp}^{1-14} = 4$ mm; d) Its mass velocities against frequencies.

combined modes. Additionally, the material's absorption curve maintains these multiple absorption peaks, although some combined ones are reduced in amplitude. The termination could be used to control the amplitude of these peaks and enhance absorption. In the next section, a constant profile associated with an ABH termination composed of three main pores at the end is studied to better understand the influence of a multiple main pore ABH termination on absorption.

3.2.2. Multiple main pores ABH termination

In this section, the previously examined constant profile is modified by reducing the radius of the last three main pores to form an ABH termination, in order to analyze their influence on low-frequency absorption through multiple combined modes. The parameters for the studied profile are defined with $r_{mp}^{1-12} = 2$ mm, $r_{mp}^{13} = 0.9$ mm, $r_{mp}^{14} = 0.7$ mm and $r_{mp}^{15} = 0.5$ mm, as represented in Fig. 6 a), and thus this material corresponds to a 4-mass-spring system.

Its absorption coefficient is shown in Fig. 6 b), according to the equivalent mass-spring model, the FEM TVA, and the experimental measurements. The three curves are very close up to 1500 Hz, with the frequency positions of the first absorption peaks being nearly identical and only minor differences in their amplitudes. At higher frequencies, similar to previous sections, some differences can be observed with a slight shift in the mass-spring model. However, it remains consistent, and the overall results are satisfactory.

The curves in the following figures are calculated solely using the

equivalent mass-spring model. In Fig. 6 c), the absorption coefficient of the studied profiles (in blue) is compared to the reference constant profile (in red) and the material corresponding only to its constant section $r_{mp}^{1-12} = 2$ mm (in dashed gray). A greater shift in absorption peaks can be observed compared to the profile from the previous section, with six absorption peaks below 2 000 Hz for this profile, compared to five for the previous profile and four for the reference profile. This is due to the fact that the ABH termination could be equivalent to a greater acoustic mass, as there are more reduced main pores, which shifts the system's resonances towards lower frequencies. Nevertheless, at the same time, this increases the losses for resonances that already had excessive losses, resulting in absorption peaks with lower amplitudes (see the second to fifth peaks in blue). Additionally, the third and fourth absorption peaks are relatively close in frequency, forming the beginning of an absorption band despite their low amplitude. Furthermore, after the resonance frequency of the cavity following the first modified main pore (the 13th), denoted as $f_{res}^{0.9mm}$ (vertical dash-dot green line), the absorption curve of the studied profile follows that of the constant section only (dashed gray). As previously mentioned, this is due to the behavior of a cavity acting as a rigid termination for frequencies beyond its resonance frequency [18,25].

The mass velocities for the profile studied in this section are plotted as a function of frequency in Fig. 6 d) and correspond to the real part of the velocities, normalized by the maximum value among them. It can be observed that beyond the sixth resonance, only the first mass has a non-

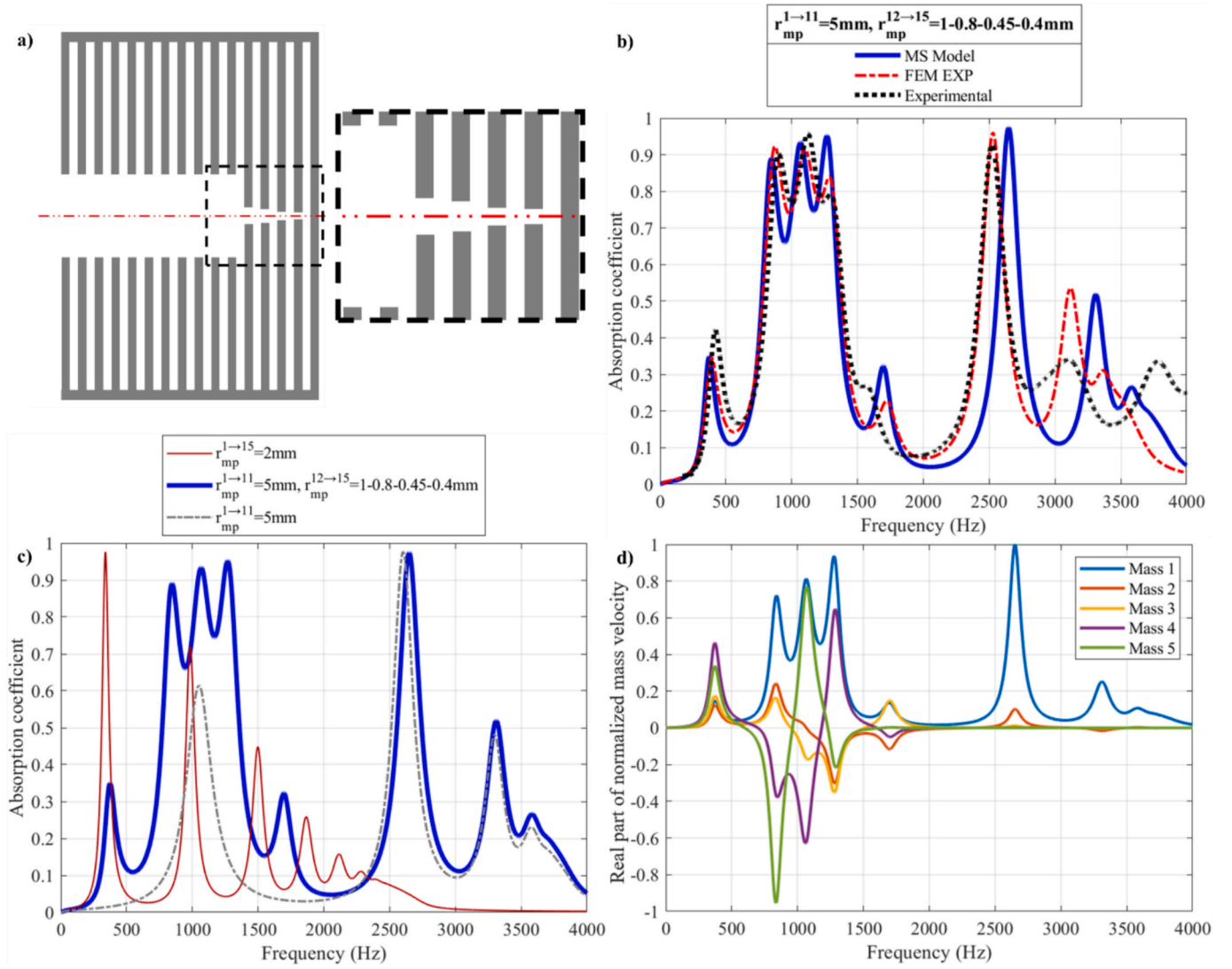


Fig. 8. a) Visualization of the first optimized metamaterial with $r_{mp}^{1 \rightarrow 11} = 5 \text{ mm}$, $r_{mp}^{12} = 1 \text{ mm}$, $r_{mp}^{13} = 0.8 \text{ mm}$, $r_{mp}^{14} = 0.45 \text{ mm}$ and $r_{mp}^{15} = 0.4 \text{ mm}$; b) Comparison of its absorption coefficient according to the equivalent mass-spring model, the FEM and experimental results; c) Comparison of its absorption coefficient with constant profile metamaterials $r_{mp}^{1 \rightarrow 15} = 2 \text{ mm}$ and $r_{mp}^{1 \rightarrow 11} = 5 \text{ mm}$; d) Its mass velocities against frequencies.

zero velocity, which corresponds well to the behavior of the constant section alone as explained in the previous paragraph. The first six resonances are influenced by all the masses and therefore correspond well to combined modes. The combined contributions of the different masses can be observed and are particularly complex for the second to fifth resonances.

Therefore, an ABH termination composed of multiple main pores accentuates the shift of absorption peaks towards lower frequencies but simultaneously reduces their amplitude due to excessive losses. To enhance the material's absorption capability, it is crucial to balance the losses to effectively utilize the low-frequency peaks from the combined modes. A constant section with fewer losses and potentially larger perforation radii could yield higher amplitude absorption peaks. Additionally, closely spaced peaks can form an effective absorption band if the peaks have high amplitudes. Nevertheless, the combined resonances depend on all the masses, making it complex to control the frequency position and amplitude of these absorption peaks for improved overall absorption. The next section focuses on optimizing the profile parameters to achieve higher amplitude absorption peaks and form absorption bands with closely spaced frequency peaks at the lowest possible frequencies.

3.3. Multi-pancake absorber with optimized ABH terminations

This section investigates multi-pancake absorber with optimized ABH terminations with multiple modified main pores at the end of a constant section to achieve a broad absorption band at low frequency without changing the material's thickness and external radius. As presented in **section 2.2**, an optimization process is employed to identify the most effective values for these parameters. Main pore profiles defined by two ($r_{mp}^{1 \rightarrow 14}$ and r_{mp}^{15}) to six ($r_{mp}^{1 \rightarrow 10}$, r_{mp}^{11} , r_{mp}^{12} , r_{mp}^{13} , r_{mp}^{14} and r_{mp}^{15}) variable parameters are considered. Multiple optimizations are performed to determine a profile featuring a broad absorption band, with a high amplitude average (exceeding 0.8) positioned at the lowest possible frequencies. The next two subsections present the optimized profiles for two different target bandwidths: a 300 Hz absorption band and a 500 Hz absorption band, both at the lowest possible frequencies.

3.3.1. Optimized metamaterial for absorption band around 300 Hz

In this section, the specified frequency bandwidth is 300 Hz, and the optimized values for the lowest frequency band result in a multi-pancake absorber with a two-parameters profile with $r_{mp}^{1 \rightarrow 14} = 4 \text{ mm}$ and $r_{mp}^{15} = 0.4 \text{ mm}$ presented in **Fig. 7 a)**. Note that multiple optimizations were

performed, and this profile exhibited a 300 Hz absorption band at lower frequencies compared to profiles with ABH terminations containing more main pores.

The absorption coefficient of this material is depicted in Fig. 7 b), showcasing a high amplitude absorption band composed of two low-frequency peaks at 599 Hz and 806 Hz. Globally, this material exhibits an absorption band between 544 Hz and 844 Hz, with an average absorption of 0.80. Moreover, between 1500 Hz and 3500 Hz, multiple narrow peaks are present. These results are validated using the FEM TVA and measurements. Below 1500 Hz, all three curves are remarkably similar. The FEM TVA and experimental curves align closely, with a slight amplitude variation for the second absorption peak compared to the equivalent mass-spring model. This discrepancy may stem from how the equivalent mass-spring model approximates the last annular cavity volume, though these differences are minor, validating the achievement of a low-frequency absorption band.

In Fig. 7 c), the optimized profile is compared with the constant reference profile profiles $r_{mp}^{1 \rightarrow 15} = 2$ mm (in red) and its constant section $r_{mp}^{1 \rightarrow 14} = 4$ mm (in dashed grey) using the equivalent mass-spring model. It is noticeable that absorption is significantly enhanced in the considered frequency bandwidth compared to the constant profiles with $r_{mp}^{1 \rightarrow 15} = 2$ mm and with $r_{mp}^{1 \rightarrow 14} = 4$ mm. At low frequencies, the absorption band is positioned between its first two frequency peaks and spans a frequency range above 300 Hz. Moreover, at higher frequencies, the profile exhibits multiple absorption peaks, with the third one reaching an amplitude exceeding 0.98 at 1904 Hz and the fourth one 0.64 at 2604 Hz. At higher frequencies, its absorption is similar to the absorption of its constant section only ($r_{mp}^{1 \rightarrow 14} = 4$ mm in dashed grey), because the last cavity has already resonated and behaves like a wall.

The velocity of the two masses representing this optimized profile is shown in Fig. 7 d). The first mass corresponds to the first main pore, while the second corresponds to the last main, r_{mp}^{15} . The first mass has a similar velocity for the first two resonances and, from the third resonance onward, behaves similarly to the reference metamaterial but with higher amplitude. The second mass shows similar velocity amplitudes for the first two resonances and minimal movement for the subsequent resonances. Thus, the first two resonances correspond to combined modes, while the following resonances are influenced only by the constant section.

Thus, with this metamaterial, the lowest possible 300 Hz absorption band is achieved using an optimized profile composed of a constant section with 14 main pores and a single smaller main pore at the end. This profile features a low-frequency absorption band with two closely spaced peaks, followed by several higher frequency absorption peaks. The next section presents a multi-pancake absorber with a second optimized profile designed to achieve a broader 500 Hz absorption band at the lowest possible frequency.

3.3.2. Optimized metamaterial for absorption band around 500 Hz

In this section, the specified frequency bandwidth is 500 Hz, and the optimized values for the lowest frequency band result in a multi-pancake absorber with a five-parameters profile with $r_{mp}^{1 \rightarrow 11} = 5$ mm, $r_{mp}^{12} = 1$ mm, $r_{mp}^{13} = 0.8$ mm, $r_{mp}^{14} = 0.45$ mm and $r_{mp}^{15} = 0.4$ mm, presented in Fig. 8 a). Note that there are no constraints on the successive decrease in the radius of the main pores in the termination.

The corresponding absorption coefficient is depicted in Fig. 8 b) showcasing a first absorption peak at 374 Hz with low amplitude, followed by a high-absorption band composed of 3 absorption peaks at 843 Hz, 1066 Hz, and 1268 Hz, then another peak at 1696 Hz with low amplitude, and finally several peaks at higher frequencies. Globally, it exhibits an average absorption coefficient of 0.80 between 782 Hz and 1282 Hz. These results are validated using the FEM TVA and measurements. Overall, below 1500 Hz, the three curves are aligned. Some differences in amplitudes are noted, but the equivalent mass-spring

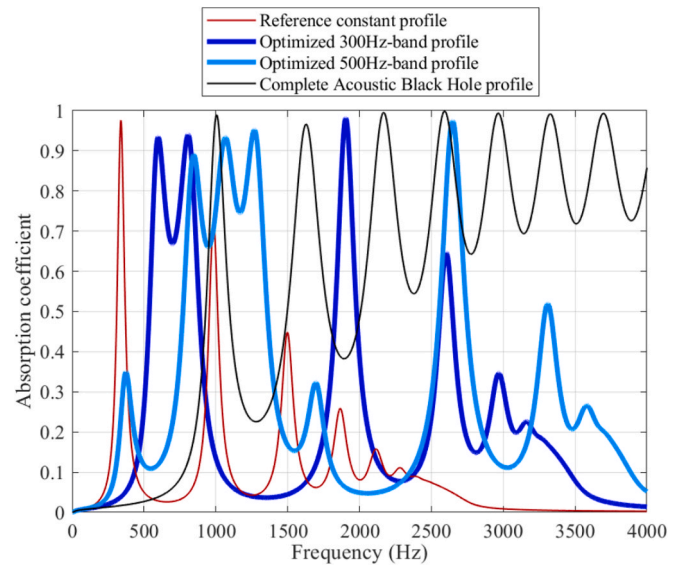


Fig. 9. Comparison of the absorption coefficient between the reference constant profile metamaterials, the optimized 300 Hz and 500 Hz-band profile metamaterials, and a complete ABH profile metamaterial from reference [18].

model remains consistent. Above 1500 Hz, the discrepancies between the FEM-TVA and experimental data may arise from the vibration of the structure's walls, and the deviation from the equivalent mass-spring model can be due to the low-frequency approximation. The results are very consistent, validating the analyses conducted in this study.

In Fig. 8 c), the absorption coefficient of the optimized profile is compared with the constant reference profile $r_{mp}^{1 \rightarrow 15} = 2$ mm (in red) and its constant section $r_{mp}^{1 \rightarrow 11} = 5$ mm (in dashed grey) using the equivalent mass-spring model. It is noticeable that absorption of the optimized metamaterial is significantly enhanced in the considered frequency bandwidth compared to the constant profiles with $r_{mp}^{1 \rightarrow 15} = 2$ mm. The first absorption peak is notably decreased, while the remaining absorption is significantly enhanced compared to the reference constant profile, and this without changing the material's thickness and external radius. The high-frequency absorption peaks appear to correspond to the secondary resonances of the constant section (see the similarity with the dashed grey curve above 1500 Hz).

The velocity of the various masses of the optimized profile is depicted in Fig. 8 d). The first mass corresponds to the first main pore, while masses 2 through 5 correspond respectively to the 12th through 15th modified main pores. It can be observed that the first five resonances correspond to combined modes involving contributions from all masses, while the following three primarily originate from the constant section, with nearly exclusive velocity of mass 1.

Therefore, an optimized profile composed of a constant section of 11 main pores and an ABH termination of four modified main pores at the end, has been identified. This profile exhibits a low-frequency absorption band with three peaks spanning just over 500 Hz. It is noteworthy that this band is broader than that of the preceding section's optimized material, albeit appearing at slightly higher frequencies.

3.3.3. Comparison with constant and ABH profiles

In Fig. 9, the absorption coefficients of the optimized profiles for the 300 Hz (in dark blue) and 500 Hz (in light blue) bands are compared with the reference profile (in red) and the complete ABH profile from a previous study [18] (in black). The complete ABH profile exhibits high absorption peaks across the frequency spectrum but forms a broad absorption band only above 2 000 Hz. In contrast, the optimized profiles achieve absorption bands at significantly lower frequencies, highlighting the capability of the studied profile, which combines a constant

section with an ABH termination, to improve low-frequency absorption. Additionally, the two optimized profiles illustrate the trade-off between the bandwidth of the absorption and its frequency position, where a lower frequency band tends to be narrower. Furthermore, compared to the reference profile, which displays primarily tonal absorption, the optimized profiles demonstrate marked improvements in low-frequency absorption while maintaining some absorption peaks at higher frequencies.

4. Conclusion

This study introduces a multi-pancake metamaterial capable of low-frequency sound absorption despite its minimal thickness. By strategically combining constant and ABH pore profiles, we demonstrate the ability to tailor the absorber's performance for desired absorption bandwidth at the lowest frequency range. A mass-spring model provides physical insights into the underlying mechanisms, revealing how ABH terminations induce lower frequency resonances and enhance absorption without increasing the material's thickness or external dimensions. Optimized designs showcase the potential for achieving broad absorption bands at low frequencies, with significant improvements compared to traditional approaches. The first optimized metamaterial exhibits a 300 Hz absorption band at low frequencies with a single main pore and ABH termination. Another optimized design, featuring a constant section of 11 main pores and an ABH termination of 4 main pores, achieves a broader absorption band of 500 Hz at slightly higher frequencies.

Appendix A

The expression of the acoustic impedance Z_{Cst} of the constant main pore section is here detailed. It is defined by

$$\begin{bmatrix} P_1 \\ P_2 \end{bmatrix} = Z_{Cst} \begin{bmatrix} V_1 \\ V_2 \end{bmatrix} \quad (\text{A.1})$$

It can be determined using the transfer matrix T_{Cst} , which relates the pressure and velocity vector at the entry and the exit as

$$\begin{bmatrix} P_1 \\ V_1 \end{bmatrix} = T_{Cst} \begin{bmatrix} P_2 \\ V_2 \end{bmatrix} \quad (\text{A.2})$$

This matrix relationship can be expanded to give the following system

$$\begin{cases} P_1 = T_{Cst;11}P_2 + T_{Cst;12}V_2 \\ V_1 = T_{Cst;21}P_2 + T_{Cst;22}V_2 \end{cases} \quad (\text{A.3})$$

Then the system can be rewritten as

$$\begin{cases} P_1 = \frac{T_{Cst;11}}{T_{Cst;21}}V_1 + \left(T_{Cst;12} - \frac{T_{Cst;11}T_{Cst;22}}{T_{Cst;21}} \right) V_2 \\ P_2 = \frac{1}{T_{Cst;21}}V_1 + \left(-\frac{T_{Cst;22}}{T_{Cst;21}} \right) V_2 \end{cases} \quad (\text{A.4})$$

For a tube of length L with a constant cross-section, the transfer matrix T_{Cst} can be expressed as

$$T_{Cst} = \begin{bmatrix} \cos(kL) & jZ\sin(kL) \\ \frac{j}{Z}\sin(kL) & \cos(kL) \end{bmatrix} \quad (\text{A.5})$$

where Z is the characteristic impedance and k_{eq} the wavenumber. Thus, the coefficients of Z_{Cst} can be expressed as

These findings offer promising avenues for developing highly efficient, thin metamaterials with practical applications in noise control and acoustic engineering.

CRediT authorship contribution statement

Gauthier Bezaçon: Writing – original draft, Visualization, Methodology, Formal analysis, Conceptualization. **Maël Lopez:** Writing – review & editing, Formal analysis, Conceptualization. **Olivier Doutres:** Writing – original draft, Supervision, Methodology, Conceptualization. **Raymond Panneton:** Writing – review & editing, Methodology. **Thomas Dupont:** Writing – original draft, Supervision, Methodology, Conceptualization.

Declaration of competing interest

The authors declare that they have no known competing financial interests or personal relationships that could have appeared to influence the work reported in this paper.

Acknowledgment

The authors acknowledge the financial support of Natural Sciences and Engineering Research 545 Council (NSERC) [funding reference numbers: RGPIN-2019-06573.

$$\left\{ \begin{array}{l} Z_{Cst;11} = \frac{\cos(kL)}{\frac{j}{Z}\sin(kL)} = -jZ\cot(kL) \\ Z_{Cst;12} = jZ\sin(kL) - \frac{\cos(kL)\cos(kL)}{\frac{j}{Z}\sin(kL)} = \frac{-\sin(kL)^2 - \cos(kL)^2}{\frac{j}{Z}\sin(kL)} = \frac{jZ}{\sin(kL)} \\ Z_{Cst;21} = \frac{1}{\frac{j}{Z}\sin(kL)} = \frac{-jZ}{\sin(kL)} \\ Z_{Cst;22} = -\frac{\cos(kL)}{\frac{j}{Z}\sin(kL)} = jZ\cot(kL) \end{array} \right. \quad (A.6)$$

and therefore, the matrix expression of Z_{Cst} is given by

$$Z_{Cst} = \begin{bmatrix} -jZ\cot(kL) & jZ/\sin(kL) \\ -jZ/\sin(kL) & jZ\cot(kL) \end{bmatrix} \quad (A.7)$$

Appendix B

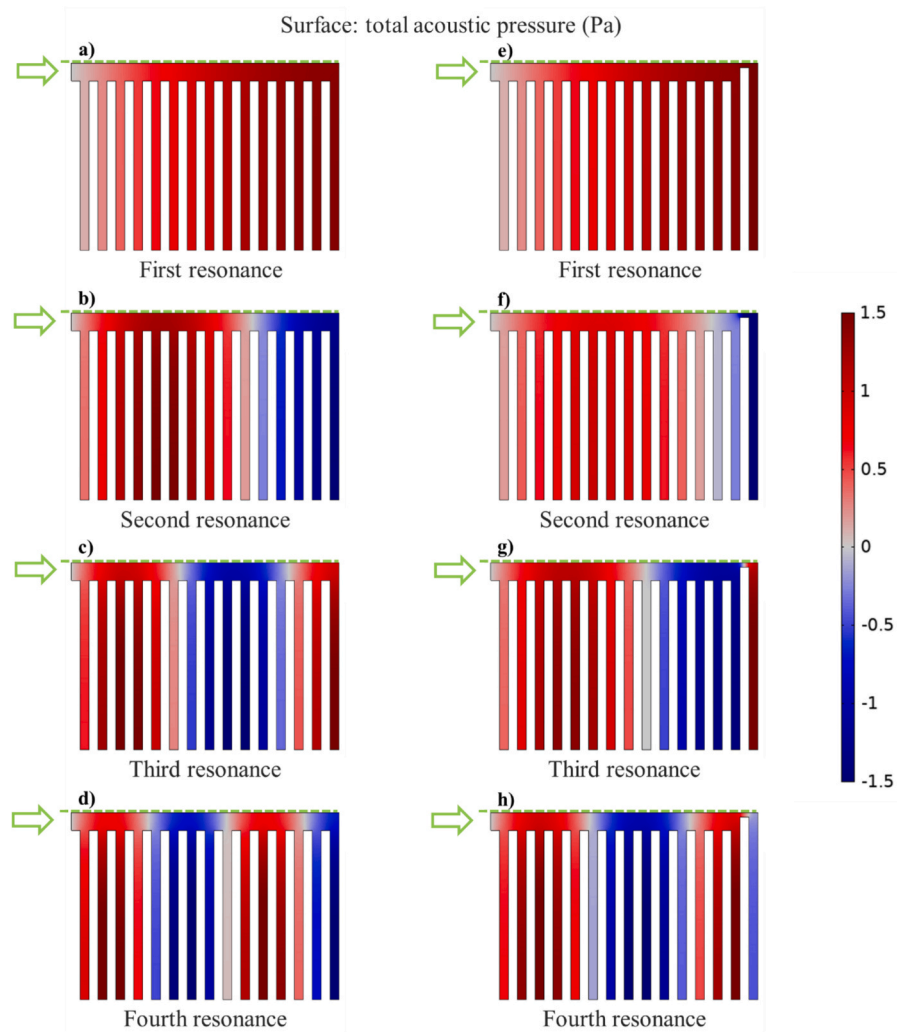


Fig. 10. Distribution of the total acoustic pressure from FEM in a 2D axisymmetric view for the first four resonances of metamaterials a-d) with a constant profile with mm, and e-h) with a smaller cavity with mm and mm.

Fig. 10 a-d) presents a visualization of the pressure field in the regular metamaterial with with $r_{mp}^{1 \rightarrow 15} = 2$ mm at the frequencies of the first four resonances, obtained by FEM in a 2D axisymmetric view. The axis of symmetry is indicated by the green dashed line, and the material's entrance is on the left, marked by the green arrow. It can be observed that there is a pressure node, and therefore a maximum acoustic velocity, at the entrance of the material (on the left) and thus for the first mass. Moreover, the material behaves like a quarter-wave resonator, with the addition of a pressure node at

each subsequent resonance.

Next, Fig. 10. e-h) shows the pressure field for the metamaterial with a single main pore termination. The distribution of the first resonance (e) is similar to that of the constant profile material (a)). However, for the second resonance (f)), the pressure node (corresponding to a maximum acoustic velocity) has shifted towards the back of the material, closer to the smaller pore, making this resonance hybrid due to the significant influence of the last main pore. For the third (g)) and fourth (h)) resonances, a pressure node is positioned at the last main pore, and their pressure distributions for the first 14 cells correspond to the second (b)) and third (c)) resonances of the constant profile material, respectively. This observation aligns with those made in Fig. 5, indicating that the material behaves similarly to one with a constant section for the resonances at higher frequencies.

Thus, the behavior of the material with a single main pore termination can also be understood by considering it as a material with 14 cells, to which an additional cavity preceded by a smaller main pore has been added. This results in the addition of an extra resonance at a lower frequency (here the second one) without significantly altering the behavior and the frequency positions of the subsequent resonances (with only a very slight shift towards higher frequencies), thereby improving its absorption at low frequencies while only slightly increasing its thickness.

Data availability

Data will be made available on request.

References

- [1] Sihvola A. Metamaterials in electromagnetics. *Metamaterials* 2007;1:2–11. <https://doi.org/10.1016/j.metmat.2007.02.003>.
- [2] Cummer SA, Christensen J, Alù A. Controlling sound with acoustic metamaterials. *Nat Rev Mater* 2016;1. <https://doi.org/10.1038/natrevmats.2016.1>.
- [3] Leclaire P, Umnova O, Dupont T, Panneton R. Acoustical properties of air-saturated porous material with periodically distributed dead-end pores. *J Acoust Soc Am* 2015;137:1772–82. <https://doi.org/10.1121/1.4916712>.
- [4] Groby J, Huang W, Lardeau A, Aurégan Y. The use of slow waves to design simple sound absorbing materials. *J Appl Phys* 2015;117:124903. <https://doi.org/10.1063/1.4915115>.
- [5] Jiménez N, Huang W, Romero-García V, Pagneux V, Groby J. Ultra-thin metamaterial for perfect and quasi-omnidirectional sound absorption. *Appl Phys Lett* 2016;109. <https://doi.org/10.1063/1.4962328>.
- [6] Jiménez N, Romero-García V, Pagneux V, Groby J. Rainbow-trapping absorbers broadband, perfect and asymmetric sound absorption by subwavelength panels for transmission problems. *Sci Rep* 2017;7. <https://doi.org/10.1038/s41598-017-13706-4>.
- [7] Huang S, Fang X, Wang X, Assouar B, Cheng Q, Li Y. Acoustic perfect absorbers via Helmholtz resonators with embedded apertures. *J Acoust Soc Am* 2019;145: 254–62. <https://doi.org/10.1121/1.5087128>.
- [8] Leblanc A, Lavie A. Three-dimensional-printed membrane-type acoustic metamaterial for low frequency sound attenuation. *J Acoust Soc Am* 2017;141: EL538-EL542. <https://doi.org/10.1121/1.4984623>.
- [9] Langfeldt F, Gleine W, Von Estorff O. An efficient analytical model for baffled, multi-celled membrane-type acoustic metamaterial panels. *J Sound Vib* 2018;417: 359–75. <https://doi.org/10.1016/j.jsv.2017.12.018>.
- [10] Abbad A, Atalla N, Ouisse M, Doutres O. Numerical and experimental investigations on the acoustic performances of membraned Helmholtz resonators embedded in a porous matrix. *J Sound Vib* 2019;459:114873. <https://doi.org/10.1016/j.jsv.2019.114873>.
- [11] Xu Q, Qiao J, Sun J, Zhang G, Li L. A tunable massless membrane metamaterial for perfect and low-frequency sound absorption. *J Sound Vib* 2021;493:115823. <https://doi.org/10.1016/j.jsv.2020.115823>.
- [12] Zhang C, Hu X. Three-Dimensional Single-Port labyrinthine acoustic metamaterial: perfect absorption with large bandwidth and tunability. *Phys Rev Appl* 2016;6. <https://doi.org/10.1103/physrevapplied.6.064025>.
- [13] Song G, Cheng Q, Huang B, Dong H, Cui T.J. Broadband fractal acoustic metamaterials for low-frequency sound attenuation. *Appl Phys Lett* 2016;109. <https://doi.org/10.1063/1.4963347>.
- [14] Gao N, Liu J, Deng J, Chen D, Huang Q, Pan G. Design and performance of ultra-broadband composite meta-absorber in the 200Hz–20kHz range. *J Sound Vib* 2023; 574:118229. <https://doi.org/10.1016/j.jsv.2023.118229>.
- [15] Dupont T, Leclaire P, Panneton R, Umnova O. A microstructure material design for low frequency sound absorption. *Appl Acoust* 2018;136:86–93. <https://doi.org/10.1016/j.apacoust.2018.02.016>.
- [16] Kone TC, Lopez M, Ghinet S, Dupont T, Panneton R. Thermoviscous-acoustic metamaterials to damp acoustic modes in complex shape geometries at low frequencies. *J Acoust Soc Am* 2021;150:2272–81. <https://doi.org/10.1121/10.0006441>.
- [17] Lopez M, Dupont T, Panneton R. Mass-spring model for acoustic metamaterials consisting of a compact linear periodic array of dead-end resonators. *J Acoust Soc Am* 2024;155(1):530–43. <https://doi.org/10.1121/10.0024212>.
- [18] Bezaçon G, Doutres O, Umnova O, Leclaire P, Dupont T. Thin metamaterial using acoustic black hole profiles for broadband sound absorption. *Appl Acoust* 2024; 216:109744. <https://doi.org/10.1016/j.apacoust.2023.109744>.
- [19] Mironov MA, Pishlyakov V. One-dimensional acoustic waves in retarding structures with propagation velocity tending to zero. *Acoust Phys* 2002;48:347–52. <https://doi.org/10.1134/1.1478121>.
- [20] Liang X, Zhou Z, Wu JH. The experimental study on low frequency sound transmission characteristics of the acoustic black hole. *Mod Phys Lett B* 2019;33: 1950458. <https://doi.org/10.1142/s021798491950458x>.
- [21] Zhang X, Li C. Broadband and low frequency sound absorption by sonic black holes with micro-perforated boundaries. *J Sound Vib* 2021;512:116401. <https://doi.org/10.1016/j.jsv.2021.116401>.
- [22] Bravo T, Maury C. Broadband sound attenuation and absorption by duct silencers based on the acoustic black hole effect: simulations and experiments. *J Sound Vib* 2023;561:117825. <https://doi.org/10.1016/j.jsv.2023.117825>.
- [23] Ou Y, Zhao Y. Design, analysis, and experimental validation of a sonic black hole structure for near-perfect broadband sound absorption. *Appl Acoust* 2024;225: 110196. <https://doi.org/10.1016/j.apacoust.2024.110196>.
- [24] Chen Y, Yu K, Fu Q, Zhang J, Lu X, Du X. A broadband and low-frequency sound absorber of sonic black holes with multi-layered micro-perforated panels. *Appl Acoust* 2024;217:109817. <https://doi.org/10.1016/j.apacoust.2023.109817>.
- [25] Umnova O, Brooke D, Leclaire P, Dupont T. Multiple resonances in lossy Acoustic Black Holes - theory and experiment. *J Sound Vib* 2023;543:117377. <https://doi.org/10.1016/j.jsv.2022.117377>.
- [26] Zhang X, He N, Cheng L, Yu X, Zhang L, Hu F. Sound absorption in sonic black holes: wave retarding effect with broadband cavity resonance. *Appl Acoust* 2024; 221:110007. <https://doi.org/10.1016/j.apacoust.2024.110007>.
- [27] Červenka M, Bednarík M. Maximizing the absorbing performance of rectangular sonic black holes. *Appl Sci* 2024;14(17):7766. <https://doi.org/10.3390/app14177766>.
- [28] Changbin G, Zhang J. Modeling and optimal design of 3 degrees of freedom Helmholtz resonator in hydraulic system. *Chin J Aeronaut* 2012;25:776–83. [https://doi.org/10.1016/s1000-9361\(11\)60444-5](https://doi.org/10.1016/s1000-9361(11)60444-5).
- [29] Jahdali RA, Wu Y. Coupled resonators for sound trapping and absorption. *Sci Rep* 2018;8. <https://doi.org/10.1038/s41598-018-32135-5>.
- [30] Duan H, Shen X, Wang E, Yang F, Zhang X, Yin Q. Acoustic multi-layer Helmholtz Resonance metamaterials with multiple adjustable absorption peaks. *Appl Phys Lett* 2021;118. <https://doi.org/10.1063/5.0054562>.
- [31] Allard JF, Atalla N. *Propagation of sound in porous media: Modelling sound absorbing materials*. 2nd ed. New York: John Wiley & Sons; 2009.
- [32] Karal FC. The analogous acoustical impedance for discontinuities and constrictions of circular cross section. *J Acoust Soc Am* 1953;25:327–34. <https://doi.org/10.1121/1.1907041>.
- [33] Romero-García V, Theocharis G, Richoux O, Pagneux V. Use of complex frequency plane to design broadband and sub-wavelength absorbers. *J Acoust Soc Am* 2016; 139:3395–403. <https://doi.org/10.1121/1.4950708>.
- [34] Dickey NS, Selamet A. Helmholtz resonators: one-dimensional limit for small length-to-diameter ratio. *J Sound Vib* 1996;195:512–7. <https://doi.org/10.1006/jsvi.1996.0440>.
- [35] ISO 10534-2:2023, *Acoustics – Determination of acoustic properties in impedance tubes Part 2: Two-microphone technique for normal sound absorption coefficient and normal surface impedance*. Geneva, Switzerland: International Organization for Standardization; 2023.